Research paper

A systematic approach to the synthesis of LDH nanoparticles by response surface methodology

Cecilia Vasti [a], Valeria Pfaffen [a], Ernesto Ambroggio [b], Mauricio R. Galiano [b], Ricardo Rojas [a,*], Carla E. Giacomelli [a]

[a] INFIQC-CONICET, Departamento de Fisicoquímica, Facultad de Ciencias Químicas, Universidad Nacional de Córdoba, Ciudad Universitaria, X5000HUA Córdoba, (Argentina)
[b] CIQUIBIC-CONICET, Departamento de Química Biológica, Facultad de Ciencias Químicas, Universidad Nacional de Córdoba, Ciudad Universitaria, X5000HUA Córdoba, (Argentina)

ARTICLE INFO

ABSTRACT

The customization of the properties of layered double hydroxides nanoparticles (LDH-NPs) is essential to optimize their design innovative systems for biomedical applications. Response surface methodologies (RSMs), a collection of mathematical and statistical techniques that allows multivariate optimization of processes, are a useful tool for LDH-NPs customization. In this work, RSMs were used to study the synthesis parameters governing the size and composition of Mg—Al LDH-NPs (Mg/Al = 3) labeled with fluorescein isothiocyanate ($FITC^{2-}$) and prepare customized samples for biological assays. The influence of $[Al^{3+}]$, $[OH^-]/[Mg^{2+}+Al^{3+}]$, $2[FITC^{2-}]/[Al^{3+}]$ and time of the hydrothermal treatment (t_{HT}) was determined by a Box-Behnken experimental design (BBD). The experimental responses were hydrodynamic diameter (d_H), polidispersity index (PI) and $FITC^{2-}$ content ($\%FITC$), and their dependence with the synthesis variables was described by polynomial model. The model correlated high $[Al^{3+}]$ with large d_H values due to aggregation processes, while t_{HT} was the main variable governing the size of the disaggregated units. These results were explained based on the precipitation and recrystallization mechanisms of LDH-NPs. The mathematical model derived from the BBD accurately predicted the synthesis conditions to obtain LDH-NPs with controlled d_H values between 50 and 200 nm, minimum PI and tunable $\%FITC$. The convenience of the synthesized LDH-NPs for biological assays were tested in experiments with giant unilamellar vesicles and cell cultures monitored by confocal microscopy.

© 2016 Elsevier B.V. All rights reserved.

1. Introduction

Layered double hydroxides (LDHs) are increasingly proposed for biomedical applications (Ladewig et al., 2010b; Chen et al., 2013; Ma et al., 2014; Kuo et al., 2015; Rojas et al., 2015) based on their synthesis in the nanometer scale, biocompatibility, anion exchange capacity, high chemical stability and pH-dependent solubility, as well as controlled release and cellular permeation capabilities (Oh et al., 2006; Rojas et al., 2015; Senapati et al., 2016). LDHs structure can be described as stacks of brucite-like layers where the isomorphic substitution of divalent (M^{2+}) by trivalent (M^{3+}) ions (e.g. M^{2+} = Mg^{2+}, Co^{2+}, Zn^{2+}; M^{3+} = Al^{3+}, Ga^{3+}, Fe^{3+}, etc.) renders layers with positive charges that are neutralized by hydrated exchangeable anions ($A^{n-}(H_2O)_m$) intercalated between them (Drits and Bookin, 2001). They can be then represented by the formula $[M^{2+}_{(1-x)}M^{3+}_x(OH)_2](A)_{1/n}\cdot mH_2O$ (m = 1–5).

Coprecipitation is the conventional method for LDH synthesis (Newman and Jones, 1998; He et al., 2006): it involves mixing metal ions (M^{2+} and M^{3+}) and base solutions in the presence of the interlayer anion (A^{n-}). To synthesize LDH nanoparticles (LDH-NPs), these solutions are rapidly mixed to maximize nucleation against particle growth, followed by the immediate separation from the synthesis media (Xu et al., 2006a). Then, LDH-NPs are dispersed in water and aged in hydrothermal conditions to enhance their disaggregation and crystallinity (Zhao et al., 2002; Xu et al., 2006b). The composition of the synthesis starting solutions (total concentration of M^{2+} and M^{3+} ions, OH^- to ($M^{2+} + M^{3+}$) ratio or A^{n-} concentration) controls particle size and distribution during the nucleation step, while temperature and time are important factors during the aging step (Xu et al., 2006a; Rojas et al., 2015). Consequently, the size of LDH-NPs can be tailored by controlling the synthesis conditions either in the nucleation or the aging step.

Response surface methodologies (RSMs) involve a statistical design of experiments devoted to the evaluation of the existing relationship between a cluster of operational variables (OVs) and measured responses of a specific process according to one or more selected criteria (Montgomery, 1991; Bezerra et al., 2008; Cuéllar et al., 2016). Multivariate experimental methods are advantageous because they allow finding the influence of each variable and their interactions to determine global optimum conditions (Nejati et al., 2015; Cuéllar et al., 2016) to

* Corresponding author.
E-mail address: rrojas@fcq.unc.edu.ar (R. Rojas).

achieve particular, preset responses. Thus, these methods have been used to optimize the synthesis conditions of nanoparticles (Wang et al., 2006) and modify the properties and composition of cationic clays such as bentonites (Meng and Yu, 2011).

The application of response surface methodology (RSM) is an attractive tool to customize the properties of LDH-NPs (Ghosal et al., 2015; Sun and Dey, 2015a). In the case of the biomedical applications of LDH-NPs (Gu et al., 2015; Sun and Dey, 2015b), the requested properties are related to the size and size distribution as these variables determine their citotoxicity (Choi et al., 2008), cellular transfection efficiency (Chen et al., 2013; Dong et al., 2014), and drug release profile (Zhang et al., 2014). In addition, highly sensitive, reliable and robust labeling methods are necessary to enable LDH-NPs tracking for cellular uptake and membrane permeation studies. Fluorescein isothiocyanate, incorporated as divalent anion ($FITC^{2-}$) between the LDH-NPs layers, has been widely used as a fluorescent label (Xu et al., 2008; Musumeci et al., 2010). On this regard, developing a model for tailoring the size and composition of LDH-NPs is useful for biological studies, and, hence, optimizing their biomedical applications (Kuthati et al., 2015; Wu et al., 2015). With this systematic approach the number of experiments needed to reach a global optimum is relatively low and the best synthesis conditions are found because the interactions between OVs are taken into account. In the light of synthesis processes, the OVs can be classified as chemical (such as the initial reagents, their concentrations and ratios) and procedural (like thermal or aging treatments) ones whereas the responses are determined by the requested properties of the synthesized particles.

In this work, we applied a RSM to optimize the synthesis of $FITC^{2-}$-labeled LDH-NPs considering the specific requirements of biological assays using a well-known coprecipitation method (Xu et al., 2006a). A Box–Behnken design was employed to statistically evaluate the effect of chemical and procedural OVs on three responses of the LDH-NPs: hydrodynamic diameter, polidispersity index and the $FITC^{2-}$ content. To predict the mathematical relationship between OVs and responses, a polynomial model was fitted to the experimental results that provided the optimal LDH-NPs properties for biological studies. Finally, the validation step comprised the synthesis of LDH-NPs in the nanometer range with minimum polydispersity and tunable fluorophore content, whose suitability was tested in biological assays with giant unilamellar vesicles and cell cultures followed by confocal microscopy.

It is worth mentioning that compared to traditional univariate methods RSM allowed tuning the properties of LDH-NPs, as well as getting a better understanding of the mechanisms involved in the synthesis procedure. In this work RSM was applied to improve the performance of LDH-NPs in biological assays, as the size, polidipersity and fluorophore contents. These features provide this work with a novel approach regarding the optimization OVs involved in LDH-NPs synthesis with the final purpose of addressing biological studies. As far as we know, such an approach has not been published in the LDH literature.

2. Materials and methods

2.1. Chemicals and solutions

Reagent grade $MgCl_2 \cdot 6H_2O$, $NaHCO_3$ (Cicarelli), NaCl (J.T. Baker), $AlCl_3 \cdot 6H_2O$, KCl, $CaCl_2$ (Anedra), sodium fluorescein isothiocyanate (Sigma-Aldrich) were used with no previous purification. Phospholipids were purchased from Avanti. The fluorescent probe BodipyTR-Ceramide was obtained from Life Technologies. ITO slides were provided by Nanocs. All solutions were prepared with purified (18 MΩ Milli Q, Millipore System) water that was decarbonated by boiling and N_2 bubbling. Unless otherwise stated, all experiments were performed at room temperature.

2.2. Synthesis and optimization methodology of LDH-NPs

(Mg, Al) LDH-NPs intercalated with chloride and labeled with $FITC^{2-}$ were prepared by a coprecipitation method at variable pH involving separate nucleation and aging steps (Xu et al., 2006a). The following solutions were mixed within 10 s under vigorous stirring: (1) a 12 mL solution of Mg^{2+} and Al^{3+}, with a 3:1 Mg/Al ratio and $[Al^{3+}] = 0.10, 0.25$ or 0.40 M, with (2) a 40 mL NaOH solution ($[OH^-]/[Mg^{2+} + Al^{3+}] = 2.00, 2.75$ or 3.50) containing the fluorescent label ($[FITC^{2-}]/[Al^{3+}] = 0, 0.10$ or 0.20). Once the addition was finished, the prepared solid was immediately separated by centrifugation from the synthesis solution and washed twice with 50 mL of water. Afterwards, the solid was dispersed in 50 mL of water and submitted to hydrothermal treatment at 80 °C for different times ($t_{HT} = 0, 4$ or 8 h). The prepared dispersions were stored in closed bottles at room temperature and used directly in the experiments. A portion of the dispersion was freeze-dried to perform the chemical and structural characterization. $[Al^{3+}]$, $[OH^-]/[Mg^{2+} + Al^{3+}]$, $[FITC^{2-}]/[Al^{3+}]$ and t_{HT} were chosen as operational values (OVs) of the synthesis procedure and 29 experiments were performed, according to the Experimental Design described in Section 2.4.

2.3. LDH-NPs characterization

Dynamic light scattering (DLS) and electrophoretic light scattering (ELS) was used to determine hydrodynamic diameter (d_H), polydispersity index (PI) and zeta potential (ζ) data, using a Delsa Nano C instrument (Beckman Coulter). d_H and PI values were calculated from the autocorrelation function ($g^{(2)}$) with the cumulants method, while electrophoretic mobilities were converted to ζ using the Smoluchowski equation. d_H, PI and ζ data are informed as the average from three determinations. Scanning electron microscopy (SEM) images were obtained in a FE-SEM Σigma instrument on samples covered with a Cr layer. The samples were prepared from the LDH-NPs dispersions, which were diluted 1:1000 in water. A drop of the diluted dispersion was placed on the holder and dried at 60 °C. C, N, and S (CNS) contents were determined using a CHN 2400 Serie II Elemental Analyzer, using cisteine as reference. $FITC^{2-}$ content (%FITC, w/w) was calculated from C content considering $FITC^{2-}$ chemical formula and molecular weight. Powder X-Ray diffraction (PXRD) patterns were recorded in a Phillips X'pert Pro instrument using a CuKα lamp (λ = 1.5408 Å) at 40 kV and 40 mA between 5° and 70° (2θ) in step mode (0.05°, 1.2 s). FT-IR spectra were measured in a Bruker IFS28 instrument using KBr pellets (1:100 sample:KBr ratio).

2.4. Experimental design

The Box–Behnken design (BBD) is a spherical, revolving RSM that consists of a central point and the middle points of the edges of the cube circumscribed on the sphere. BBD is a class of rotatable or nearly rotatable second-order design based on three-level, incomplete factorial designs. The number of experiments (N) required for BBD development is defined as $N = 2k(k-1) + C_0$, where k is the number of OVs and C_0 is the number of central point (Ferreira et al., 2007). A second order polynomial model was fitted to the experimental results to obtain the mathematical relationship between independent OVs and dependent response. Then, the relationship between response and OVs was formulated as:

$$Y = \beta 0 + \sum_{i=1}^{k} \beta_i x_i + \sum_{i=1}^{k} \beta_{ii} x_i^2 + \sum_{i=1}^{k-1} \sum_{j=2}^{k} \beta_{ij} x_i x_j + \varepsilon \tag{1}$$

where Y is the predicted response, β_0 is the offset term, β_i are coefficients of linear effect, β_{ii} are coefficients of squared effect, β_{ij} are coefficients of interaction effect, and ε is the random error (Eq. (1)).

In this study, the optimization process of the LDH-NPs synthesis was carried out using BBD for the four OVs above mentioned ($[Al^{3+}]$, $[OH^-]/[Mg^{2+}+Al^{3+}]$, $[FITC^{2-}]/[Al^{3+}]$ and t_{HT}). The range of these four parameters were chosen based on our preliminary experiments and on the literature (Xu et al., 2006a; Ladewig et al., 2010a). It led to 24 factorial points and 5 replicates at the center point to allow the estimation of pure error, indicating that altogether 29 experiments were required (Table 1). d_H, PI and %FITC were chosen as the responses to be modeled.

Design-Expert 7.0.0 software was employed to generate experimental designs, statistical analyses, and regression models. The adequacy of the developed models was tested by the coefficient of determination (R^2) and its statistical significance was checked by a Fisher F-test. The level of significance was given as values of the probability (p-value) < 0.05.

2.5. LDH-NPs optimization for biological assays

The validation of the model was performed by determining the optimal OVs to synthesize LDH-NPs with controlled particle size (around 50, 100 and 150 nm), low PI (<0.25) and customizable FITC (between 3 and 7% depending of the fluorescence needed for the experiments). Three different preset responses were selected and the corresponding syntheses were carried out with the OVs selected (Table 2).

Giant unilamellar vesicles (GUVs) and cells (RAW264.7) were selected to evaluate the convenience of the synthesized LDH-NPs for biological assays. GUVs containing 80% palmytoiloleoyl phosphatidylcholine (POPC) and 20% palmitoyloleoyl phosphatidylserine (POPS) were synthesized on ITO slides using the classical electroformation technique (Wesolowska et al., 2009). Briefly, 10 μL of a 0.5 mg/mL lipid stock solution of POPC:POPS (4:1 mol ratio; solvent: chloroform/methanol 2:1 (v/v)) with 0.2% of the fluorescent lipid BodipyTR-Ceramide was spread onto two ITO-coated slides (electroformation electrodes). The slides were submitted to vacuum for 4 h to eliminate the traces of organic solvent. GUVs formation, in sucrose solutions matching the osmolarity of the buffer Tris-HCl 50 mM pH 7.4, was performed for 40 min under a sinusoidal potential of 1 V and 10 Hz and at room temperature. GUVs were incubated with LDH-NPs dispersions at a concentration of 100 μg/mL in Tris-HCl 50 mM pH 7.4 for 10 min. As a control experiment, GUVs was incubated with 5 μM $FITC^{2-}$ in the same conditions. Confocal images were performed on a LSM 5 PASCAL (Zeiss).

The cell line RAW264.7 was bought from ATCC and expanded from the initial into a master cell bank. Cells were maintained in Dulbecco's modified eagle medium (DMEM) supplemented with 10% fetal bovine serum, 200 U/mL penicillin and 100 μg/mL streptomycin (all from Invitrogen). Cells were grown in a humidified incubator at 37 °C and 5% CO_2. For the uptake experiments, cells were seeded at a density of 50,000 cells/cm². On the following day, the cells were washed twice with buffer Tris-HCl 50 mM (pH 7.4) and incubated with LDH-NPs dispersions at a concentration of 100 μg/mL for 4 h. Following incubation, cells were washed twice with pre-warmed Tris-HCl 50 mM and fixed with 1% paraformaldehyde during 5 min at 4 °C. Nuclei were stained with Hoechst 33258 and then coverslips were mounted on glass slides using Fluorsave reagent (Merck Millipore). Confocal images were performed on a FluoView 300 Confocal Microscope (Olympus).

Table 2
Validation experiments performed according to the responses polynomial models.

Responses	Validation experiment		
	I	II	III
Predicted d_H (nm)	50	104	153
Prediction range (nm)	40–60	80–130	120–180
Experimental d_H (nm)	58	115	140
Predicted PI	0.16	0.20	0.20
Prediction range	0.07–0.32	0.08–0.44	0.10–0.37
Experimental PI	0.14	0.19	0.25
Predicted % FITC	3.3	7.1	5.3
Prediction range	1.9–4.6	5.7–8.5	4.0–6.5
Experimental %FITC	3.6	6.6	4.7
Operational variables (OVs)			
$2[FITC^{2-}]/[Al^{+3}]$	0.05	0.20	0.15
$[OH^-]/[Mg^{2+}+Al^{3+}]$	2.25	2.50	2.75
$[Al^{3+}]$ (M)	0.10	0.10	0.25
t_{HT} (h)	2	6	6

Table 1
Operational variables (OVs) and responses of the BBD runs for LDH-NPs synthesis.

Run	$2[FITC^{2-}]/[Al^{+3}]$	$[OH^-]/[Mg^{2+}+Al^{3+}]$	$[Al^{3+}]$ (M)	t_{HT}(h)	d_H (nm)	PI	%FITC
1	0	3.50	0.25	4	6586	1.50	0
2	0.10	2.75	0.25	4	113	0.21	3.2
3	0.10	2.75	0.25	4	109	0.14	3.1
4	0.20	3.50	0.25	4	158	0.23	4.1
5	0.10	3.50	0.25	0	390	0.31	3.4
6	0.20	2.75	0.40	4	12,915	3.34	4.4
7	0.10	2.00	0.25	0	48	0.26	3.2
8	0.10	3.50	0.10	4	90	0.12	3.3
9	0	2.75	0.25	0	88	0.21	0
10	0.10	2.00	0.10	4	75	0.26	4.6
11	0.10	2.75	0.25	4	128	0.20	3.1
12	0.20	2.75	0.25	8	121	0.17	4.0
13	0.10	2.00	0.40	4	19,748	6.01	5.2
14	0.10	2.75	0.10	0	47	0.23	3.2
15	0.10	2.75	0.10	8	95	0.25	7.9
16	0.10	2.75	0.25	4	128	0.11	2.4
17	0.10	2.75	0.40	0	2685	0.85	2.8
18	0	2.75	0.10	4	102	0.17	0
19	0	2.00	0.25	4	71	0.19	0
20	0.10	2.75	0.40	8	2587	0.06	2.9
21	0	2.75	0.25	8	122	0.12	0
22	0.10	3.50	0.25	8	1813	0.20	3.2
23	0.20	2.75	0.25	0	2738	0.90	4.1
24	0.10	2.00	0.25	8	813	0.33	4.1
25	0.20	2.00	0.25	4	4150	0.70	6.2
26	0.10	3.50	0.40	4	4152	1.10	2.8
27	0.10	2.75	0.25	4	137	0.24	2.7
28	0	2.75	0.40	4	6038	1.46	0
29	0.20	2.75	0.10	4	96	0.22	4.8

3. Results and discussion

3.1. Optimization of the LDH-NPs synthesis

As described in the Experimental Section, four operational variables (OVs) were chosen to optimize the synthesis of LDH-NPs: $[Al^{3+}]$, $[OH^-]/[Mg^{2+}+Al^{3+}]$, $2[FITC^{2-}]/[Al^{3+}]$ and t_{HT}. On the other hand, d_H, PI and %FITC data were used as responses to be modulated from the LDH-NPs synthesis. The experimental conditions of the 29 runs of the BBD are included in Table 1, together with the responses measured for each one of them. The d_H values measured for the different runs of the BBD varied greatly (from 47 nm to a few μm). Values above 400 nm were not due to a larger size of individual LDH-NPs but to their aggregation. Since LDH-NPs dispersions are stabilized by electrostatic repulsions, the aggregation process was enhanced when LDH-NPs presented ζ values below 35 mV (Supporting Information, Fig. S1), while high ζ values are associated to low d_H regions.

To determine the main significant effects of the OVs, an analysis of the variance (ANOVA) was conducted. For the data analysis, d_H values above 400 nm were rescaled per $d_H' = 400 + d_H/10$ to minimize the aggregation effect. This correction allowed keeping the values of the aggregated nanoparticles above 400 nm and minimized their weight in the fitting, which diminished their effect in the study of the non-aggregated samples. The ANOVA analysis (Tables S1 and S2 for d_H and PI data analysis, respectively) showed the linear and interactive relationships between the OVs and the responses. The significance of each term was assessed according to their p-values. The ANOVA indicated that the polynomial models were highly significant at probability level $p < 0.0001$ for the response. The lack of fit p-values was 0.3155 and 0.7647 for d_H and PI, respectively, which indicated an appropriate fitting between responses and the OVs (Bia et al., 2014; Cuéllar et al., 2016). After removing insignificant effects in coded values, the following polynomial models were obtained for d_H (Eq. (2)) and PI (Eq. (3)):

$$
\begin{aligned}
1/\sqrt{d_H} =\ & 0.08281388 + 1.248783X_1 + 0.0318461X_2 \\
& + 1.96073138X_3 - 0.06999943X_4 - 0.526481X_1X_2 \quad (2) \\
& - 3.145086X_1X_3 - 0.049461X_1X_4 - 0.63587281X_2X_3 \\
& + 0.3895001X_2X_4 + 0.01802053X_3X_4 - 6.6868X_1^2 \\
& - 0.00709376X_2^2 - 4.89161422X_3^2 + 0.00027061X_4^2 \\
& + 1.3527X_1^2X_2 + 0.5X_1^2X_4 + 0.120619X_1X_2^2 \\
& + 5.870548X_1X_3^2 - 0.00606041X_2^2X_4 + 1.40494812X_2X_3^2
\end{aligned}
$$

$$
\begin{aligned}
1/(PI+1)^3 =\ & 1.739165038 \\
& + 3.9985487X_1 - 0.593723935X_2 - 11.85953515X_3 \quad (3) \\
& - 0.06830646X_4 - 9.0241638X_1X_2 + 3.2366014X_1X_3 \\
& - 0.330987X_1X_4 + 11.35962727X_2X_3 + 0.017844102X_2X_4 \\
& + 0.14866568X_3X_4 - 42.1178X_1^2 - 0.041652518X_2^2 \\
& - 11.80917343X_3^2 - 13.05851X_1^2X_2 - 117.00157X_1^2X_3 \\
& + 2.68069X_1^2X_4 + 2.6412961X_1X_2^2 + 41.0852252X_1X_3^2 \\
& - 2.107588676X_2^2X_3
\end{aligned}
$$

where $\times_1$ is $2[FITC^{2-}]/[Al^{3+}]$, $\times_2$ is $[OH^-]/[Mg^{2+}+Al^{3+}]$, $\times_3$ is $[Al^{3+}]$ and $\times_4$ is t_{HT}.

The goodness of the fit was checked by the coefficient of determination (R^2). The R^2 values of 0.994 and 0.969 (Tables S1 and S2) are in good agreement with the experimental results, indicating that 99.4 and 96.9% of the variability can be predicted by the model for d_H and PI, respectively. Consequently, the models were expected to predict the range that included the experimental responses measured for newly synthesized samples with preset values of the OVs. The validation of the predictive capacity of the model is discussed in Section 3.2.

Fig. 1 shows the response contours of d_H polynomial model expressed by Eq. (1) in the absence of $FITC^{2-}$ (% FITC = 0) at three $[Al^{3+}]$. Only d_H values below 400 nm were measured for $[Al^{3+}] = 0.10$ mol L^{-1} independently of the values of the other OVs whereas at $[Al^{3+}] = 0.40$ mol L^{-1}, the area with d_H values above 400 nm dominated the contour, which indicated that mainly aggregated particles were obtained at high $[Al^{3+}]$. Finally, the points for $[Al^{3+}] = 0.25$ mol L^{-1} were located in an intermediate region and d_H values increased steeply with increasing $[OH^-]/[Mg^{2+}+Al^{3+}]$. Similar results were obtained at higher %FITC values and, consequently, $[Al^{3+}] = 0.10$ mol L^{-1} was selected as optimal OV for attaining $FITC^{2-}$-labeled LDH-NPs.

The size and polydispersity of LDH-NPs were controlled by their coprecipitation and recrystallization mechanisms (Sun and Dey, 2015a, 2015b; Galvão et al., 2016). LDH-NPs are primarily nucleated as amorphous nanoparticles with sizes below 100 nm. These particles have a lower number of high-energy sites (i.e., charged sites) per unit surface area compared to the thermodynamically stable crystalline counterpart and, consequently, they are heavily aggregated (Sun and Dey, 2015b). When the particles are washed and dispersed in water, a portion of the particles, determined by their solubility products (Boclair and Braterman, 1999), are dissolved and thermodynamically stable LDH-NPs are formed due to the recrystallization processes (Navrotsky, 2011; Sun and Dey, 2015a). These processes are enhanced by aging of LDH-NPs under hydrothermal conditions and they lead to larger LDH-NPs units with a higher concentration of surface charged sites, which hindered their aggregation. The aggregation of LDH-NPs
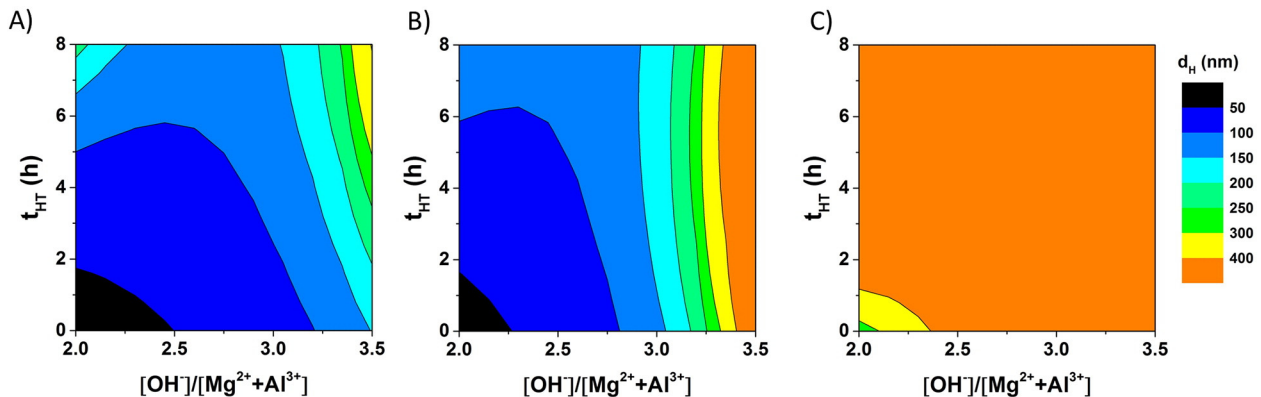

Fig. 1. Response contours (scale in nm) of the hydrodynamic diameter (d_H) polynomial model expressed by Eq. (1). The response contours were obtained for 11 × 11 matrixes obtained at $2[FITC^{2-}]/[Al^{3+}] = 0$ and $[Al^{3+}] = 0.10$ (A); 0.25 (B) or 0.40 mol L^{-1} (C).

at high $[Al^{3+}]$ was then assigned to the high particle concentration in the resulting dispersions. Therefore, the fraction of dissolved solid was lower, which hindered the recrystallization processes. Also, high pH values inhibit LDH-NPs dissolution-recrystallization processes, which explained the increasing aggregation with increasing $[OH^-]/$ $[Mg^{2+}+Al^{3+}]$ at $[Al^{3+}] = 0.25$ M.

Contrarily, t_{HT} was the main tool to minimize the particles aggregation and control the particle size of LDH-NPs, as demonstrated by Fig. 2, which shows the dependence of d_H and PI polynomial models with t_{HT}, $[OH^-]/[Mg^{2+}+Al^{3+}]$, and $2[FITC^{2-}]/[Al^{3+}]$ at $[Al^{3+}] = 0.10$ mol L^{-1}. In agreement with the literature (Musumeci et al., 2010; Dong et al., 2015), the model indicated a general particle size increment with

increasing t_{HT} (Fig. 2, left). On the other hand, there was a crossed interaction between $2[FITC^{2-}]/[Al^{3+}]$ and $[OH^-]/[Mg^{2+}+Al^{3+}]$: the lowest d_H values were obtained when both OVs were in the maximum or the minimum, while when one of them was in the maximum and the other one in the minimum, d_H reached the highest value. According to the polynomial model, the particle size of LDH-NPs can be tailored between 50 and 100 nm at $t_{HT} = 0$ by controlling $2[FITC^{2-}]/[Al^{3+}]$ and $[OH^-]/[Mg^{2+}+Al^{3+}]$. On the other hand, this range was enlarged up to 400 nm by regulating t_{HT}. Besides controlling the average particle size of LDH-NPs, minimizing the width of the size distribution is a mandatory requirement to prepare nanoparticles with controlled properties. The PI values (Fig. 2, right) decreased with increasing t_{HT}, while
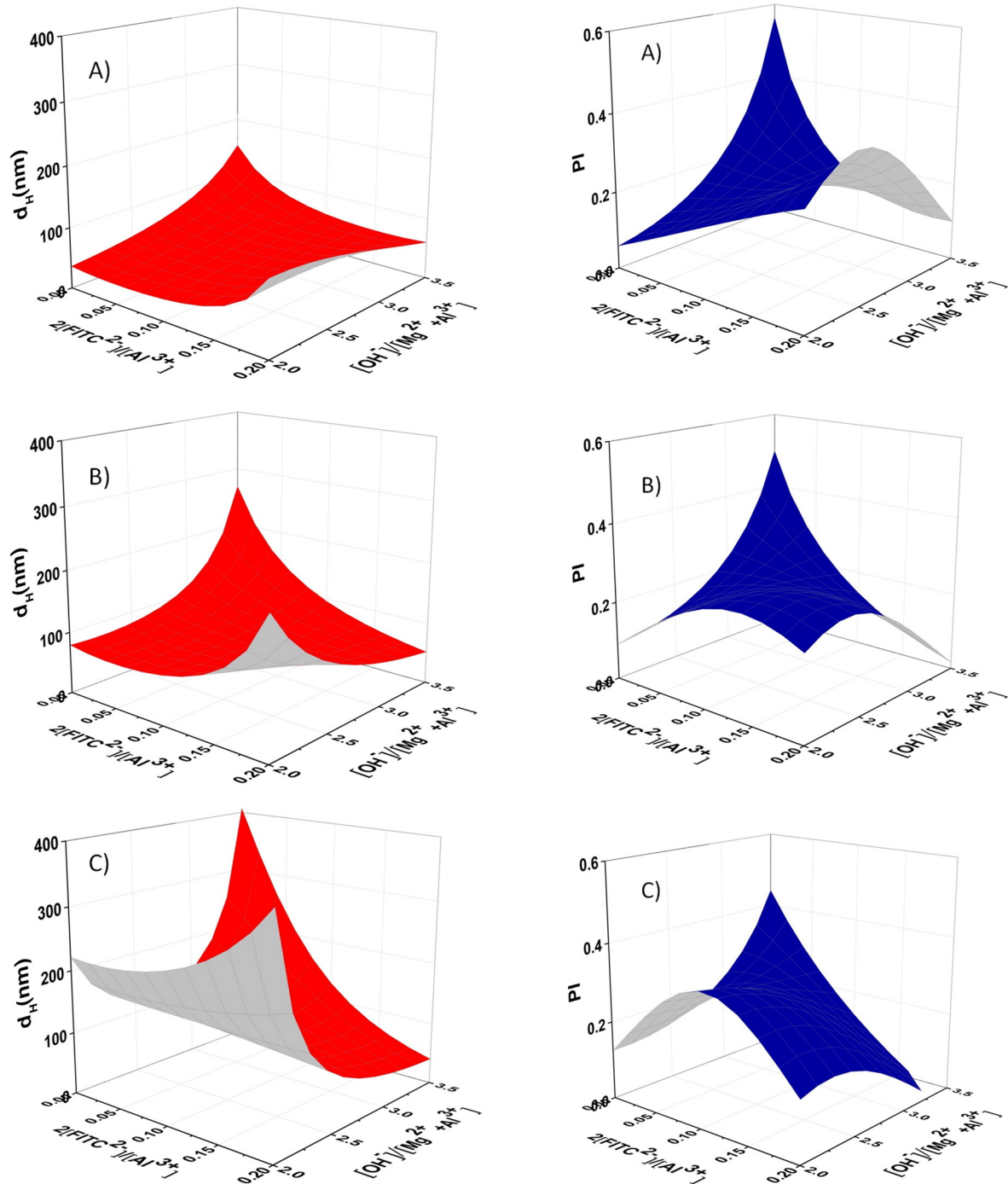

Fig. 2. Response surface of the hydrodynamic diameter (d_H) and the polidispersity (PI) polynomial models expressed by Eqs. (1) and (2), respectively. The response surfaces were obtained for 11 × 11 matrixes obtained at (A) $t_{HT} = 0$ h; (B) $t_{HT} = 4$ h (C) $t_{HT} = 8$ h. $[Al^{3+}] = 0.10$ M.

$2[FITC^{2-}]/[Al^{3+}]$ and $[OH^-]/[Mg^{2+}+Al^{3+}]$ showed a parallel effect to that observed for d_H values. The lowest *PI* values were obtained when both OVs were in their minimum or maximum values simultaneously and, contrarily, *PI* values rose when decreasing one of the OVs while increasing the other one.

The actual morphology of the particles are exemplified in Fig. 3, which includes size distribution plots and SEM images of LDH-NPs prepared at $[Al^{3+}] = 0.10$ mol L^{-1} and $t_{HT} = 4$ h. In all cases the nanoparticles were disc-shaped, with ill-defined edges. In general, the size distribution reflected in the morphology of the particles shown in the SEM images. However, with the less monodisperse sample (run 29) there was some discrepancy regarding the amount of small and large particles. In fact, DLS measurements of polydisperse dispersions are dominated by the larger particles due to the lower light scattering capacity of the smaller ones.

Finally, FITC^{2-} content (*%FITC*) was also evaluated as a response and subjected to data analysis. The ANOVA analysis (Table S3) showed that the polynomial model was highly significant at probability level ($p < 0.0001$) for the response and the statistical significance of the model was checked by F-test. The polynomial model to predict the *%FITC* values of the prepared LDH-NPs (Eq. (4)) was:

$$Y_3 = 13.5233121 + 83.2153083X_1 - 9.07327368X_2 - 11.169311X_3 \quad (4)$$
$$- 9.71498898X_1X_2 - 123.723992X_1^2 + 1.63830436X_2^2$$
$$+ 20.9574843X_3^2$$

where $\times_1$ is $2[FITC^{2-}]/[Al^{3+}]$; $\times_2$, $[OH^-]/[Mg^{2+}+Al^{3+}]$, and $\times_3$, $[Al^{3+}]$. On the other hand, *%FITC* showed no dependence with t_{HT}. R^2 value (0.961) denoted a high significance of the model.

Fig. 4 shows the dependence of *%FITC* polynomial model, expressed by Eq. (3), with $[OH^-]/[Mg^{2+}+Al^{3+}]$, and $2[FITC^{2-}]/[Al^{3+}]$ at $[Al^{3+}] = 0.10$ mol L^{-1}. As expected, *%FITC* increased with increasing $2[FITC^{2-}]/[Al^{3+}]$, while the $[OH^-]/[Al^{3+}]$ effect was related to competition of FITC^{2-} and OH$^-$ anions for LDH anion exchange sites. Also, surface deprotonation reactions of hydroxyl groups diminished the particle charge and the anion exchange capacity of LDH-NPs (Rojas et al., 2011; Giacomelli and Rojas, 2015). On the other hand,
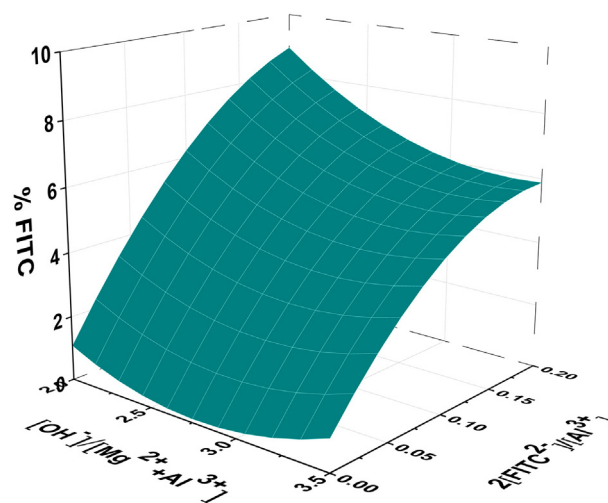

Fig. 4. Response surface of the FITC^{2-} content (*%FITC*) polynomial model expressed by Eq. (3). The response surface was obtained for 11×11 matrix measured at $[Al^{3+}] = 0.1$ mol L^{-1} and $t_{HT} = 4$ h.

t_{HT}, contrarily to that of d_H and *PI*, present no significant effect in FITC^{2-} incorporation. FITC^{2-} incorporation was produced without changing the ζ values of the synthesized LDH-NPs (Fig. S1B), which indicated that the FITC^{2-} were attached exclusively by electrostatic interactions and/or located between the LDH layers (Rojas et al., 2014). The PXRD patterns of LDH-NPs (Supporting Information Fig. S2) showed peaks corresponding to LDH phases with basal spacing around 8.1 Å, due to the intercalation of chloride anions. A larger spacing was expected for LDH-NPs containing FITC^{2-} because of the dye size(Xu et al., 2008). However, the low loading (up to 20% of chloride replaced by the dye) resulted in negligible changes in the average interlayer spacing.

3.2. Validation of the model

To verify the suitability of the defined polynomial models, three validation experiments were carried out with the appropriate OVs that
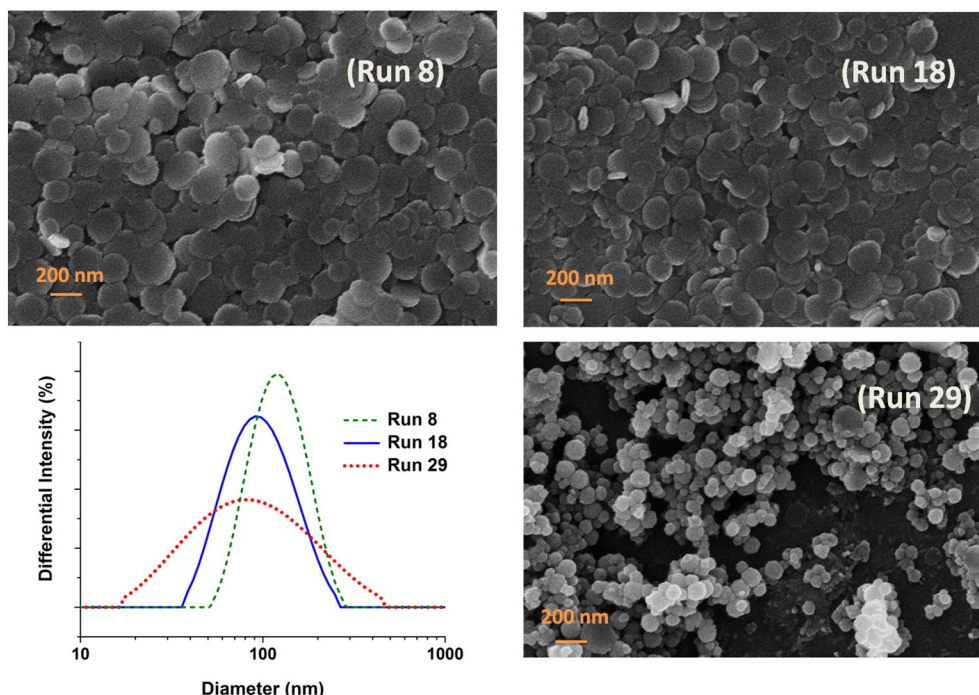

Fig. 3. Particle size distribution in intensity and SEM images of runs 8, 14 and 29. The responses of the corresponding runs are marked in bold letters in Table 1.

gave the optimum responses for the biological assays with GUVs or cells. In general, particles with d_H values ranging from 50 nm to 200 nm and a low PI (below 0.25) are preferred for biomedical applications(Nel et al., 2009) whereas $FITC^{2-}$ content depends on the studied biological target (GUVs or cells). To reach appropriate signals in the confocal microscope, the fluorophore content in GUVs experiments was kept low because the images were taken directly from the suspensions containing the labeled LDH-NPs in the presence of GUVs. On the other hand, cell experiments involved several washing steps demanding higher fluorophore content in the initial labeled LDH-NPs suspensions. Hence, $\%FITC=$ values of 3 and 7 were selected to produce a suitable fluorescence at LDH-NPs for GUVs or cells, respectively. These constraints were used to validate the ability of the polynomial models to predict the range where d, PI and $\%FITC$ values are included for LDH-NPs prepared by selected synthesis conditions.

Table 2 compares the experimental d, PI and $\%FITC$ values to the predicted range of values obtained from the polynomial models for the different validation experiments. In all cases, the experimental results

were found within the predicted range for all the responses, confirming that the developed models were able to predict the selected responses. Then, the model allowed optimizing the synthesis of LDH-NPs in the nanometer range with a narrow size distribution as well as tunable $FITC^{2-}$ contents by changing OVs, such as t_{HT}, $2[FITC^{2-}]/[Al^{3+}]$ and $[OH^-]/[Al^{3+}]$ for $[Al^{3+}] = 0.10$ mol L^{-1}. Even $[Al^{3+}]$ can be modulated within certain range, as demonstrated by the validation experiment III ($[Al^{3+}] = 0.25$ mol L^{-1})

3.3. Interaction of LDH-NPs with GUVs and cells

The suitability of the synthesized LDH-NPs for biological assays was determined in experiments with GUVs and a cell line (RAW264) followed by confocal microscopy (Fig. 5). GUVs are micrometric scale liposomes enclosing an internal aqueous environment and bounded by a single phospholipid bilayer membrane (Walde et al., 2010). Consequently, they display a set of physical features (size, lipid structure and control of the internal content) that closely replicates, albeit in a
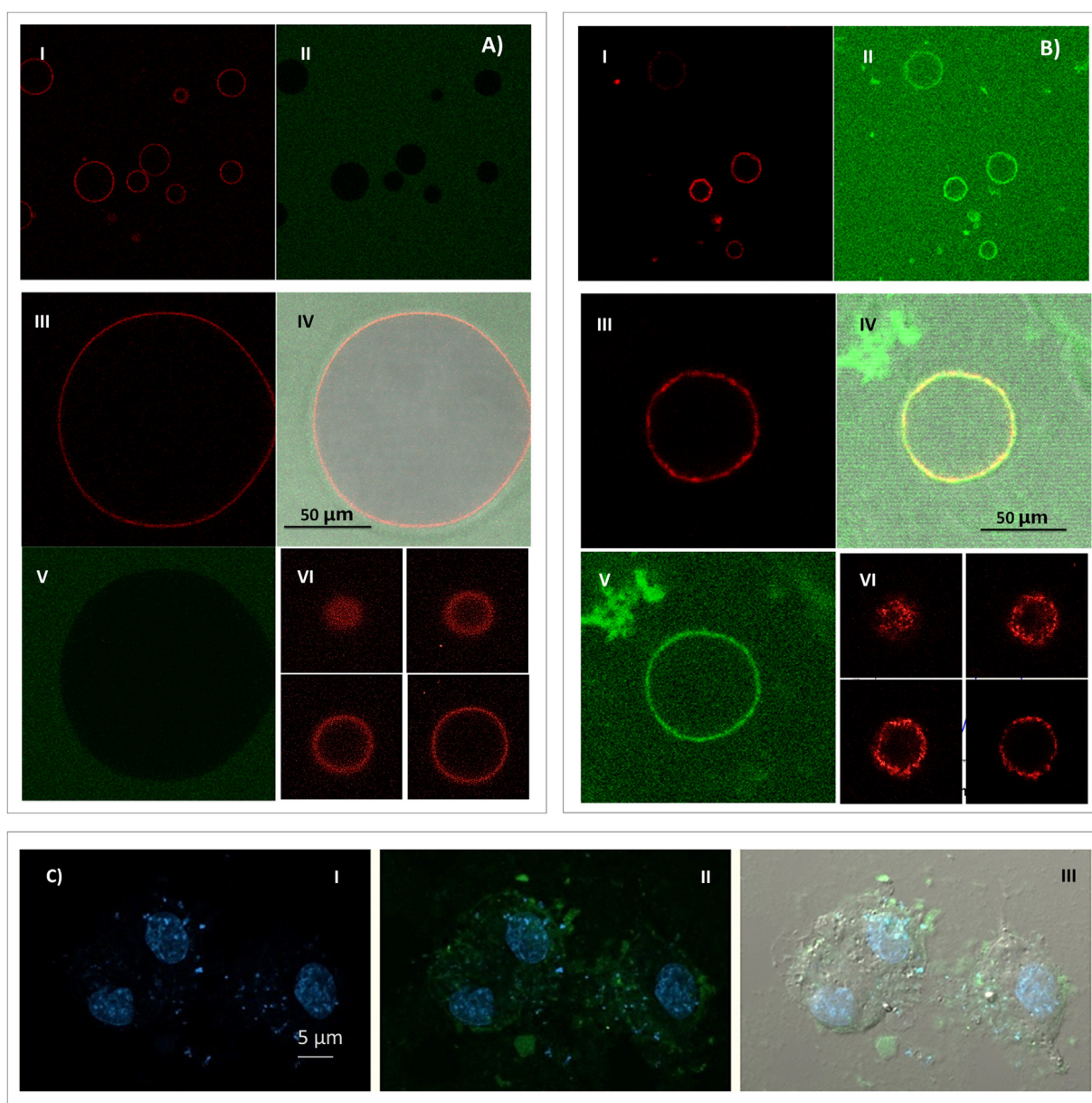

Fig. 5. Confocal images of (A) GUVs incubated with fluorescein(B) and labeled LDH-NPs (validation experiment I) (C). Cellular uptake of labeled LDH-NPs (validation experiment II) after 4 h of incubation.

more simplified manner, the structural organization of cellular membranes (Matosevic, 2012). Compared to other systems that imitate biological membranes, GUVs are less prone to develop artifacts than, for example, supported bilayers, and they resemble cell membranes more closely than lipid monolayers do (Juhasz et al., 2012). The main benefit of GUVs is the possibility of distinguishing the physicochemical interactions from the biological ones.

Fig. 5A shows a control experiment where the GUVs, marked with the fluorescent lipid BodipyTR-Ceramide (red), were placed in a medium containing only $FITC^{2-}$. Panels I and II show the general view of the GUVs in this medium, while panels III to V display a single vesicle, representative of the global behavior of the system. The red channel images, corresponding to the membrane marker emission (Panels I and III), indicate that spherical GUVs with smooth surface were prepared, and panel VI demonstrate that the membrane marker was homogeneously distributed in the whole structure. Conversely, the green channel, corresponding to $FITC^{2-}$ emission (panels II, V), shows no fluorescence inside the GUVs, indicating the low membrane permeation capacity of free $FITC^{2-}$. Finally, the colocalization image (panel IV), indicates that there was no accumulation of free $FITC^{2-}$ at the GUVs membrane.

On the other hand, Fig. 5B shows the same experiment in the presence of $FITC^{2-}$-labeled LDH-NPs. LDH-NPs with low % FITC (validation experiment I) were used to avoid saturation of the fluorescence detector. Red channel images (panels I and III) displayed an uneven distribution of the membrane marker owing to a change in the lipidic structure of the membrane (panel VI). In addition, $FITC^{2-}$ signal was detected inside the GUVs (Panels II and V), which pointed to an increased vesicle permeability in the presence of LDH-NPs. Finally, the colocalization image (panel IV) demonstrates that LDH-NPs were accumulated at the GUVs surface. LDH-NPs were then responsible for the uneven lipidic structure of the GUVs membrane and the consequent increased permeability. This result emphasized the importance of the attractive electrostatic interactions between the positively charged $FITC^{2-}$-labeled LDH-NPs and the negatively charged membrane of the GUVs ($\zeta = -15.4 \pm 0.5$ mV in small POPC/POPS vesicles ($d = 120$ nm) in identical media conditions). Thus, LDH-NPs accumulated on the surface of the GUVs, causing the uneven redistribution of the anionic lipids fraction of the membrane and the concomitant increase in their permeability.

The LDH-NPs with high $FITC^{2-}$ content (validation experiment II) were used to measure cell internalization in culture medium (Fig. 5C). Nucleus marker (blue channel, Panel I) and phase-contrast (panel III) images indicate that the morphology of the cells was maintained after incubation in the presence of LDH-NPs for 4 h. On the other hand, $FITC^{2-}$ emission image (panel II) shows that LDH-NPs were internalized by these cells. This result was in good agreement with that found in the literature (Gu et al., 2011; Chen et al., 2013; Dong et al., 2014) and the increasing permeability of biological membranes exposed by the experiments with GUVs.

4. Conclusions

In this study, a Box–Behnken design was used to optimize and study the effects of chemical ($[Al^{3+}]$, $[OH^-]/[Mg^{2+}+Al^{3+}]$ and $[FITC^{2-}]/[Mg^{2+}+Al^{3+}]$) and procedural (aging time, t_{HT}) operational variables (OVs) on the particle size, polidispersity and $FITC^{2-}$ content of LDH-NPs. The experimental data were fitted by polynomial models that, represented as response surfaces, allowed estimating both the individual and interactive effects of the OVs. The aggregation of LDH-NPs increased with $[Al^{3+}]$ while the size of the individual platelets increased with t_{HT}, which was explained by the coprecipitation and recrystallization mechanism of LDH-NPs. The model also allowed the incorporation of FITC in a controllable manner, while the positive ζ values measured for FITC containing samples indicated that this incorporation was not preferentially produced at the particle surface. The model validation was performed on the synthesis conditions to prepare optimized LDH-NPs for

biomedical assays: controlled size (between 50 and 200 nm), low polidispersity and tunable $FITC^{2-}$ content. The concordance between the experimental data and the calculated responses was optimal, which confirmed the good predictive capacity of the polynomial model. Then, response surface methodologies demonstrated to be a useful tool to customize the properties of LDH-NPs. In the case of biological assays, it allowed obtaining determining the interactions between LDH-NPs and giant unilamellar vesicles, which gives insights about the physical interactions between LDH-based nanocarriers and cells.

Appendix A. Supplementary data

Hydrodynamic diameter and %*FITC* vs. zeta potential curves, structural characterization (PXRD patterns and FT-IR spectra) of the LDH-NPs, and ANOVA results for the fittings of d, PI and %*FITC* responses are available free of charge as online content. Supplementary data associated with this article can be found in the online version, at 10.1016/j.clay.2016.12.023.

References

Bezerra, M.A., Santelli, R.E., Oliveira, E.P., Villar, L.S., Escaleira, L.A.A., 2008. Response surface methodology (RSM) as a tool for optimization in analytical chemistry. Talanta 76:965–977. http://dx.doi.org/10.1016/j.talanta.2008.05.019.

Bia, G., Borgnino, L., Ortiz, P.I., Pfaffen, V., 2014. Chemical multivariate optimization of square wave voltammetry using bismuth film electrode to determine atrazine. Sensors Actuators B Chem. 203:396–405. http://dx.doi.org/10.1016/j.snb.2014.07.003.

Boclair, J.W., Braterman, P.S., 1999. Layered double hydroxide stability. 1. Relative stabilities of layered double hydroxides and their simple counterparts. Chem. Mater. 11: 298–302. http://dx.doi.org/10.1021/cm980523u.

Chen, M., Cooper, H.M., Zhou, J.Z., Bartlett, P.F., Xu, Z.P., 2013. Reduction in the size of layered double hydroxide nanoparticles enhances the efficiency of siRNA delivery. J. Colloid Interface Sci. 390:275–281. http://dx.doi.org/10.1016/j.jcis.2012.09.033.

Choi, S.-J., Oh, J.-M., Choy, J.-H., 2008. Safety aspect of inorganic layered nanoparticles: size-dependency in vitro and in vivo. J. Nanosci. Nanotechnol. 8:5297–5301. http://dx.doi.org/10.1166/jnn.2008.1143.

Cuéllar, M., Pfaffen, V., Ortiz, P.I., 2016. Application of multi-factorial experimental design to successfully model and optimize inorganic chromium speciation by square wave voltammetry. J. Electroanal. Chem. 765:37–44. http://dx.doi.org/10.1016/j.jelechem.2015.07.050.

Dong, H., Chen, M., Rahman, S., Parekh, H.S., Cooper, H.M., Xu, Z.P., 2014. Engineering small MgAl-layered double hydroxide nanoparticles for enhanced gene delivery. Appl. Clay Sci. 100:66–75. http://dx.doi.org/10.1016/j.clay.2014.04.028.

Dong, H., Parekh, H.S., Xu, Z.P., 2015. Particle size- and number-dependent delivery to cells by layered double hydroxide nanoparticles. J. Colloid Interface Sci. 437:10–16. http://dx.doi.org/10.1016/j.jcis.2014.09.010.

Drits, V.A., Bookin, A.S., 2001. Crystal structure and X-ray identification of layered double hydroxides. In: Rives, V. (Ed.), Layered Double Hydroxides: Present and Future. Nova Science, New York, pp. 39–92.

Ferreira, S.L.C., Bruns, R.E., Ferreira, H.S., Matos, G.D., David, J.M., Brandão, G.C., da Silva, E.G.P., Portugal, A.A., dos Reis, P.S., Souza, A.S., dos Santos, W.N.L., 2007. Box-Behnken design: an alternative for the optimization of analytical methods. Anal. Chim. Acta 597:179–186. http://dx.doi.org/10.1016/j.aca.2007.07.011.

Galvão, T.L.P., Neves, C.S., Caetano, A.P.F., Maia, F., Mata, D., Malheiro, E., Ferreira, M.J., Bastos, A.C., Salak, A.N., Gomes, J.R.B., Tedim, J., Ferreira, M.G.S., 2016. Control of crystallite and particle size in the synthesis of layered double hydroxides: macromolecular insights and a complementary modeling tool. J. Colloid Interface Sci. 468:86–94. http://dx.doi.org/10.1016/j.jcis.2016.01.038.

Ghosal, P.S., Gupta, A.K., Ayoob, S., 2015. Effect of formation pH, molar ratio and calcination temperature on the synthesis of an anionic clay based adsorbent targeting de fluoridation. Appl. Clay Sci. 116–117:120–128. http://dx.doi.org/10.1016/j.clay.2015.08.026.

Giacomelli, C.E., Rojas, R., 2015. Size-tunable LDH-protein hybrids toward the optimization of drug nanocarriers. J. Mater. Chem. B 3:2778–2785. http://dx.doi.org/10.1039/C4TB01992J.

Gu, Z., Rolfe, B.E., Thomas, A.C., Campbell, J.H., Lu, G.Q.M., Xu, Z.P., 2011. Cellular trafficking of low molecular weight heparin incorporated in layered double hydroxide nanoparticles in rat vascular smooth muscle cells. Biomaterials 32:7234–7240. http://dx.doi.org/10.1016/j.biomaterials.2011.05.083.

Gu, Z., Zuo, H., Li, L., Wu, A., Xu, Z.P., 2015. Pre-coating layered double hydroxide nanoparticles with albumin to improve colloidal stability and cellular uptake. J. Mater. Chem. B 3:3331–3339. http://dx.doi.org/10.1039/C5TB00248F.

He, J., Wei, M., Kang, Y.-G., Evans, D.G., Duan, X., 2006. Preparation of layered double hydroxides. In: Evans, D.G., Duan, X. (Eds.), Layered Double Hydroxides. Springer-Verlag, Berlin, pp. 89–119.

Juhasz, J., Davis, J.H., Sharom, F.J., 2012. Fluorescent probe partitioning in GUVs of binary phospholipid mixtures: implications for interpreting phase behavior. Biochim. Biophys. Acta Biomembr. 1818:19–26. http://dx.doi.org/10.1016/j.bbamem.2011.09.006.

Kuo, Y.-M., Kuthati, Y., Kankala, R.K., Wei, P.-R., Weng, C.-F., Liu, C.-L., Sung, P.-J., Mou, C.-Y., Lee, C.-H., 2015. Layered double hydroxide nanoparticles to enhance organ-specific targeting and the anti-proliferative effect of cisplatin. J. Mater. Chem. B 3:3447–3458. http://dx.doi.org/10.1039/C4TB01989J.

Kuthati, Y., Kankala, R.K., Lee, C., 2015. Layered double hydroxide nanoparticles for biomedical applications: current status and recent prospects. Appl. Clay Sci. 112–113:100–116. http://dx.doi.org/10.1016/j.clay.2015.04.018.

Ladewig, K., Niebert, M., Xu, Z.P., Gray, P.P., Lu, G.Q., 2010a. Controlled preparation of layered double hydroxide nanoparticles and their application as gene delivery vehicles. Appl. Clay Sci. 48:280–289. http://dx.doi.org/10.1016/j.clay.2009.11.032.

Ladewig, K., Niebert, M., Xu, Z.P., Gray, P.P., Lu, G.Q.M., 2010b. Efficient siRNA delivery to mammalian cells using layered double hydroxide nanoparticles. Biomaterials 31:1821–1829. http://dx.doi.org/10.1016/j.biomaterials.2009.10.058.

Ma, R., Wang, Z., Yan, L., Zhu, G., 2014. Novel Pt-loaded layered double hydroxide nanoparticles for efficient and cancer-cell speci f i c delivery of a cisplatin prodrug†. J. Mater. Chem. B 2:4868–4875. http://dx.doi.org/10.1039/c4tb00645c.

Matosevic, S., 2012. Synthesizing artificial cells from giant unilamellar vesicles: state-of-the art in the development of microfluidic technology. BioEssays 34:992–1001. http://dx.doi.org/10.1002/bies.201200105.

Meng, R., Yu, X., 2011. Investigation of ultrasound assisted regeneration of Ni-bentonite with response surface methodology (RSM). Appl. Clay Sci. 54:112–117. http://dx.doi.org/10.1016/j.clay.2011.06.015.

Montgomery, D.C., 1991. Design and Analysis of Experiments. John Wiley & Sons, Ltd., New York.

Musumeci, A.W., Mortimer, G.M., Butler, M.K., Xu, Z.P., Minchin, R.F., Martin, D.J., Ping, Z., Minchin, R.F., Martin, D.J., 2010. Fluorescent layered double hydroxide nanoparticles for biological studies. Appl. Clay Sci. 48:271–279. http://dx.doi.org/10.1016/j.clay.2009.11.008.

Navrotsky, A., 2011. Nanoscale effects on thermodynamics and phase equilibria in oxide systems. ChemPhysChem 12:2207–2215. http://dx.doi.org/10.1002/cphc.201100129.

Nejati, K., Keypour, H., Nezhad, P.D.K., Asadpour-zeynali, K., Rezvani, Z., 2015. Experimental design for the optimization of the synthesis conditions of Zn—Al-layered double hydroxides nanoparticles based on X-ray diffraction data. Mol. Cryst. Liq. Cryst. 608:177–189. http://dx.doi.org/10.1080/15421406.2014.940261.

Nel, A.E., Mädler, L., Velegol, D., Xia, T., Hoek, E.M.V., Somasundaran, P., Klaessig, F., Castranova, V., Thompson, M., 2009. Understanding biophysicochemical interactions at the nano-bio interface. Nat. Mater. 8:543–557. http://dx.doi.org/10.1038/nmat2442.

Newman, S.P., Jones, W., 1998. Synthesis, characterization and applications of layered double hydroxides containing organic guests. New J. Chem. 22:105–115. http://dx.doi.org/10.1039/a708319j.

Oh, J.-M., Choi, S.-J., Kim, S.-T., Choy, J.-H., 2006. Cellular uptake mechanism of an inorganic nanovehicle and its drug conjugates: enhanced efficacy due to clathrin-mediated endocytosis. Bioconjug. Chem. 17:1411–1417. http://dx.doi.org/10.1021/bc0601323.

Rojas, R., Bruna, F., de Pauli, C.P., Ulibarri, M.Á., Giacomelli, C.E., 2011. The effect of interlayer anion on the reactivity of Mg—Al layered double hydroxides: improving and extending the customization capacity of anionic clays. J. Colloid Interface Sci. 359:136–141. http://dx.doi.org/10.1016/j.jcis.2011.03.056.

Rojas, R., Jimenez-Kairuz, A.F., Manzo, R.H., Giacomelli, C.E., 2014. Release kinetics from LDH-drug hybrids: effect of layers stacking and drug solubility and polarity. Colloids Surf. A Physicochem. Eng. Asp. 463:37–43. http://dx.doi.org/10.1016/j.colsurfa.2014.09.031.

Rojas, R., Aristizabal Bedoya, D., Vasti, C., Giacomelli, C.E., 2015. LDH nanoparticles: synthesis, size control and applications in nanomedicine. In: Sherman, I.T. (Ed.), Layered Double Hydroxides (LDHs). Nova Press, New York, pp. 101–120.

Senapati, S., Thakur, R., Verma, S.P., Duggal, S., Mishra, D.P., Das, P., Shripathi, T., Kumar, M., Rana, D., Maiti, P., 2016. Layered double hydroxides as effective carrier for anticancer drugs and tailoring of release rate through interlayer anions. J. Control. Release http://dx.doi.org/10.1016/j.jconrel.2016.01.016.

Sun, X., Dey, S.K., 2015a. Insights into the synthesis of layered double hydroxide (LDH) nanoparticles: part 2. Formation mechanisms of LDH. J. Colloid Interface Sci. 458:160–168. http://dx.doi.org/10.1016/j.jcis.2015.06.025.

Sun, X., Dey, S.K., 2015b. Insights into the synthesis of layered double hydroxide (LDH) nanoparticles: part 1. Optimization and controlled synthesis of chloride intercalated LDH. J. Colloid Interface Sci. 459:264–272. http://dx.doi.org/10.1016/j.jcis.2015.06.025.

Walde, P., Cosentino, K., Engel, H., Stano, P., 2010. Giant vesicles: preparations and applications. Chembiochem 11:848–865. http://dx.doi.org/10.1002/cbic.201000010.

Wang, H.-C., Wu, C.-Y., Chung, C.-C., Lai, M.-H., Chung, T.-W., 2006. Analysis of parameters and interaction between parameters in preparation of uniform silicon dioxide nanoparticles using response surface methodology. Ind. Eng. Chem. Res. 45:8043–8048. http://dx.doi.org/10.1021/ie060299f.

Wesolowska, O., Michalak, K., Maniewska, J., Hendrich, A.B., 2009. Giant unilamellar vesicles — a perfect tool to visualize phase seperation and lipid rafts in model systems. Acta Biochim. Pol. 56, 33–39 20091772. [pii].

Wu, Y., Zhu, R., Zhou, Y., Zhang, J.J., Wang, W., Sun, X., Wu, X., Cheng, L., Zhang, J.J., Wang, S., 2015. Layered double hydroxide nanoparticles promote self-renewal of mouse embryonic stem cells through the PI3K signaling pathway. Nanoscale 7:11102–11114. http://dx.doi.org/10.1039/C5NR02339D.

Xu, Z.P., Stevenson, G., Lu, C.-Q., Lu, G.Q.M., 2006a. Dispersion and size control of layered double hydroxide nanoparticles in aqueous solutions. J. Phys. Chem. B 110:16923–16929. http://dx.doi.org/10.1021/jp062281o.

Xu, Z.P., Stevenson, G.S., Lu, C.-Q., Lu, G.Q.M., Bartlett, P.F., Gray, P.P., 2006b. Stable suspension of layered double hydroxide nanoparticles in aqueous solution. J. Am. Chem. Soc. 128:36–37. http://dx.doi.org/10.1021/ja056652a.

Xu, Z.P., Niebert, M., Porazik, K., Walker, T.L., Cooper, H.M., Middelberg, A.P.J., Gray, P.P., Bartlett, P.F., Lu, G.Q.M., 2008. Subcellular compartment targeting of layered double hydroxide nanoparticles. J. Control. Release 130:86–94. http://dx.doi.org/10.1016/j.jconrel.2008.05.021.

Zhang, X.-Q., Zeng, M.-G., Li, S.-P., Li, X.-D., 2014. Methotrexate intercalated layered double hydroxides with different particle sizes: structural study and controlled release properties. Colloids Surf. B: Biointerfaces 117C:98–106. http://dx.doi.org/10.1016/j.colsurfb.2014.02.018.

Zhao, Y., Li, F., Zhang, R., Evans, D.G., Duan, X., 2002. Preparation of layered double-hydroxide nanomaterials with a uniform crystallite size using a new method involving separate nucleation and aging steps. Chem. Mater. 14:4286–4291. http://dx.doi.org/10.1021/cm020370h.